Spectroscopic and Superparamagnetic Behaviour of Hausmannite Manganese Oxide Nanoparticles

S. Karpagavalli[1,*], S. John Kennady Vethanathan[2] and S. Perumal[3]

[1]Department of Physics, Govindammal Aditanar College for Women (Affiliated to Manonmaniam Sundaranar University, Tirunelveli), Tiruchendur-628215, India
[2]Department of Physics, St. Johns College, Palayamkottai-627002, India
[3]Department of Physics, Noorul Islam College of Arts and Science, Kumaracoil-629301, India

*Corresponding author: E-mail: karthikabharthi@gmail.com

Hausmannite manganese oxide (Mn_3O_4) nanoparticles are synthesized by microwave assisted solvothermal method. The calcination temperature of manganese oxide was determined from TG-DTA analysis. The structural characteristics of as prepared Mn_3O_4 nanoparticles are analyzed by powder X-ray diffraction. The Fourier transform infrared analysis is used to identify molecular structural changes of the manganese oxide sample. The SEM images revealed the surface morphology of the Mn_3O_4 nanoparticles and determined the size of the particle to be in the range of 30-40 nm. UV-visible spectrum showed that pure Mn_3O_4 nanoparticle exhibits maximum absorption at 396 nm. The cyclic voltammetry studies are used to evaluate specific capacitance and electrochemical behaviour of Mn_3O_4 nanoparticles. The magnetic properties of Mn_3O_4 nanoparticles are examined by vibrating sample magnetometer.

Keywords: Mn_3O_4 nanoparticles, Solvothermal method, Electrochemical studies.

INTRODUCTION

The discovery of nanomaterials triggered an intense research and development activities because of their enhanced physical properties and a huge potential for development of processes and applications at low dimensions [1]. The size of the particle is of the order of a few nanometers to a few hundred nanometers that evolves fascinating optical, electrical, electrochemical, magnetic and catalytic properties. Metallic oxides exhibit interesting electrical, electrochemical and magnetic properties due to changes in structure and bonds. At present, many types of transition metals and metal oxides nanoparticles are used in various fields such as physics, chemistry, biology and in materials science. Compared to bulk active electrode materials, the corresponding nanomaterials possess more excellent electrochemical activity such as higher capacities, larger surface areas and lower current densities, thereby; nanomaterials have potential applications in electrochemical and magnetic fields. Many properties are continuously modified as a function of system size [2,3].

Among the metal oxides, manganese oxides can be considered the most complex of the metallic elements. Manganese

oxides have been different applications like electrodes for lithium-ion batteries, catalysts, soft magnetic materials, high density magnetic storage media, ion exchangers, sensors, molecular absorption and electronics. Manganese is a transition metal and has many oxidation states (+2, +3, +4) and can give many phases of manganese oxides like MnO, MnO_2, Mn_2O_3, Mn_3O_4 and metastable Mn_5O_8. These oxides could co-exist or progressively change one into another during the oxidation process, which is usually controlled by the diffusion of oxygen. Because of different oxidation states, manganese has attracted many research efforts. Manganese oxides are non-toxic, abundant and cost-effective and have a wide range of technical applications including catalytic, electrochemical, magnetic, optical and electrocatalytic sensors. Mn_3O_4 is a black mineral hausmannite at ambient temperature has a distorted spinel structure with tetragonal distortion due to John-Teller effect on Mn^{3+}. In the $Mn^{2+}[Mn_2^{3+}]O_4^{2-}$ structure the Mn^{2+} and Mn^{3+} ions occupy the octahedral and tetrahedral sites respectively. As a mixed valent transition metal oxide, Mn_3O_4 is particularly important.

One of the difficult tasks is in the synthesis of metal oxide nanoparticles that consists in getting monodisperse nanoparticles.

Besides, it is essential to control over the size of the nanoparticles and to know its exact composition. For manganese oxides, the most important task is to synthesize a single phase because in almost all methods exists core-shell structures [4].

In manganese ions, Mn^{2+} is rather stable in acidic atmosphere, it quickly oxidised by air. A weak environment is required for the preparation of Mn_3O_4 nanoparticles [5,6]. The natural abundance of Mn_3O_4 and its environmental affinity make it a promising electrode material for use in various energy-storage mechanisms. Mn_3O_4 has favourable pseudo capacitive characteristics [7]. Magnetic Mn_3O_4 nanoparticles show remarkable new theory such as high field irreversibility, high saturation field, superparamagnetism and anisotropy contributions. These phenomena arise from narrow and finite-size effects and surface effects that dominates the magnetic behaviour of individual nanoparticles [8].

Toufiq *et al.* [9] synthesized MnO_2 nanowires and analyzed the optical and magnetic properties of MnO_2 nanowires. The energy band gap value of Mn_3O_4 is 2.5 eV calculated from UV-visible absorption studies. The magnetic measurement represents the antiferromagnetic behaviour of manganese oxide nanowires [9]. Sherin and Thomas [10] reported the synthesis of MnO_2, crystallite size 23 nm determined by using powder XRD and magnetic measurements. Shokoohi *et al.* [11] investigated optical characteristics of manganese tetraoxide nanoparticles. Ali *et al.* [12] revealed the electrochemical behaviour of MnO_2 nanoflower that possesses very good capacitive behaviour.

In the present work, nanocrystalline Mn_3O_4 nanoparticles are synthesized by microwave assisted solvothermal method. The structural, electrochemical and magnetic properties of as-synthesized nanoparticles are characterized by TG-DTA, powder XRD, FTIR, SEM, UV-visible, CV and VSM.

EXPERIMENTAL

Microwave assisted solvothermal method: All the reagents are of analytical grade (AR) and used without further purification. Manganese acetate tetrahydrate ($Mn(CH_3COO)_2·4H_2O$) and urea (H_2NCONH_2) are used as precursors. Ethylene glycol ($C_2H_6O_2$) is used as solvent. Manganese acetate tetrahydrate was dissolved in ethylene glycol, the solution is stirred well for 2 h using magnetic stirrer. The mixed solution kept in a microwave oven, the microwave irradiation is carried out till the solvent evaporates completely. The prepared brown precipitates are washed with double distilled water and acetone two or three times to remove unwanted organic impurities. The synthesized brown products are filtered and dried in an oven at 50 °C [13].

Characterization: The thermogravimetry analysis and differential thermal analysis (TG-DTA) of the samples were taken using (Perkin-Elmer, Diamond). The TGA analysis was performed in the temperature range 40 to 700 °C at a heating rate of 10 °C/min under nitrogen atmosphere. The structural characteristics are examined by the use of powder X-ray diffraction (XRD) (Bruker AXS D8 Advance model diffractometer using CuK_α (λ = 0.15406 nm) radiation. The functional groups present in the material were examined by Fourier transform infrared spectroscopy (FTIR) (Shimadzu Model–IR Affinity-1) in the wavenumber range 4000-400 cm^{-1}. The morphology of the as-prepared sample is tested by scanning electron microscope (SEM) (JEOL Model JSM-6390LV). The optical properties are analyzed by ultraviolet-visible spectrometer (Model: Varian, Cary 5000) in the wavelength range 200-800 nm. The electrochemical properties are examined by (Princeton Applied Research-2 channels) frequency range 1 Hz to 1 MHz magnetic study was carryout by using vibrating sample magnetometer (VSM) (Model: LakeShore 7410).

RESULTS AND DISCUSSION

Thermogravimetry analysis/differential thermal analysis (TG/DTA): Thermogravimetry analysis of the manganese oxide was carried out to determine the decomposition temperature and the rate of decomposition. TGA/DTA curves of manganese oxide samples are depicted in Fig. 1 (a) and (b).

Thermal analysis displays three important regions where the decomposition takes place. The first region (40 to 250 °C) corresponds to the evolution of physisorbed and structural water until 250 °C. It showed that some manganese ions could have to move interlayer region and increase the hydration energy because they bound very strongly the interlayer water molecules. The second region and the third region (250 to 350 °C) corresponds to phase change to Mn_3O_4. These materials
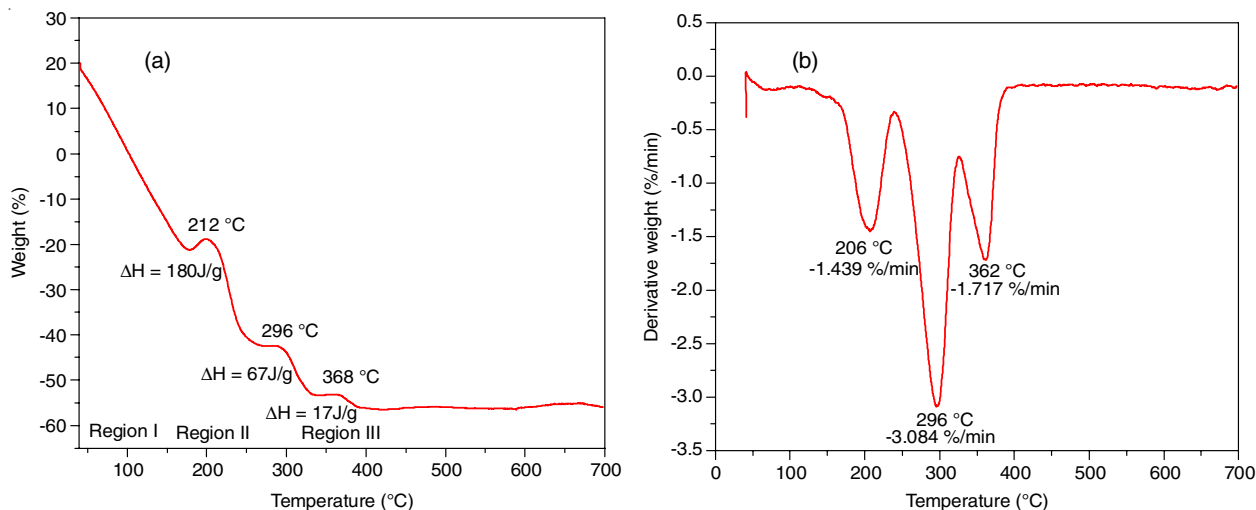

Fig. 1. (a) TG and (b) DTA curves for manganese oxide nanoparticles

highly thermally stable at 400 °C, they lose 20 % of weight [14-16].

$$3Mn(CH_3COO)_2 \cdot 4H_2O + (CH_2OH)_2 + H_2NCONH_2 \xrightarrow{\ \blacktriangle\ }$$
$$Mn_3O_4 + 6CH_3COOH + 2CH_3OH$$

From TGA-DTA results, the brown coloured samples anneal to a high temperature 400 °C in a muffle furnace for 1 h, to obtain Mn_3O_4 Nanoparticles. The calcination temperature is observed for Mn_3O_4 is 400 °C.

Structural characterization by powder X-ray diffraction analysis: X-ray diffraction pattern of Mn_3O_4 nanoparticles are presented in Fig. 2. The sharp intense peaks in XRD pattern exhibit the synthesized samples were highly crystalline in nature. All the observed peaks are well indexed to tetragonal crystal structure. The diffraction peaks at 2θ angles of 29°, 32.4°, 36°, 38.1°, 44.4°, 45.3°, 50.8°, 53.7°, 56.1°, 58.5°, 59.8°, 64.8° and 74.04° corresponds to the (h k l) planes are (112), (103), (211), (004), (220), (213), (105), (312), (303), (321), (224), (400) and (413) set to tetragonal spinel structure and the space group of (Mn_3O_4) Hausmannite is 141/amd. The obtained results are in good agreement with the JCPDS file number 80-0382 [17].
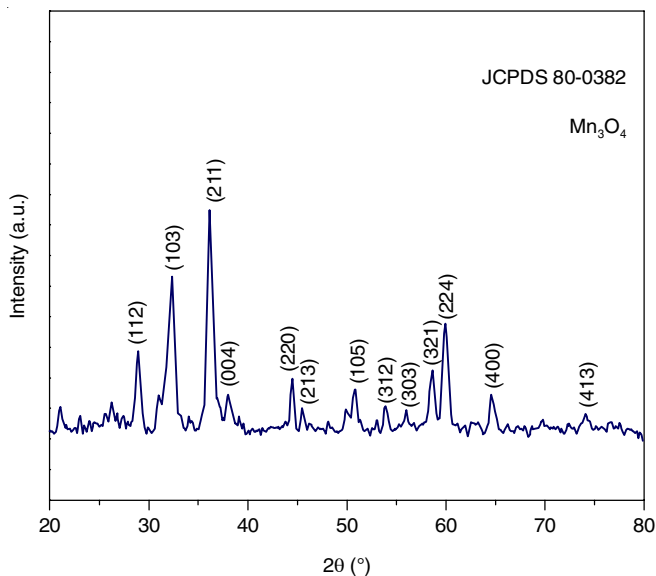

Fig. 2. XRD pattern of Mn_3O_4 (tetragonal spinel structure) nanoparticles

Williamson and Hall (W-H) proposed a method for finding size and strain broadening by looking at the peak width as a function of 2θ. W-H plot is plotted with 4 sin θ/kλ on the x-axis and βcos θ/kλ on the y-axis. From this linear fit, inverse of particle size and strain are extracted from the y-intercept and slope respectively. Fig. 3 shows W-H plot for pure Mn_3O_4 nanoparticles [18]. The estimated particle size nearly agreed wih Debye's result. From this W-H plot, it is observed that small strain and has negligible effect in X-ray diffraction broadening.
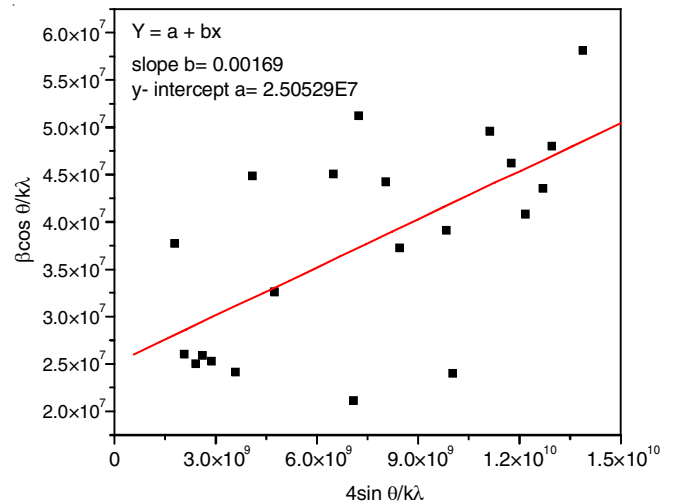

Fig. 3. W-H plot for pure Mn_3O_4 nanoparticles

From Debye Scherrer's equation and W-H plot, the average crystallite size was estimated and the lattice parameters, volume, bond length and strain of the nanoparticles are calculated and listed in Table-1.

Fourier transform infrared spectral analysis: The FTIR spectrum of Mn_3O_4 nanoparticles is shown in Fig. 4. In this spectrum, the absorption bands in the range of 400-700 cm^{-1} denotes the stretching and bending vibrations of $[MnO]_n$ [10]. FTIR absorption bands of Mn_3O_4 nanoparticles were exhibited in the spectrum with the bands 667, 615, 527 and 412 cm^{-1}. The vibrational frequency located at 667 and 615 cm^{-1} are the characteristics of Mn-O stretching modes in tetrahedral sites [19]. The bands at 527 and 412 cm^{-1} are corresponds to the distortion vibration of Mn-O in an octahedral sites [20,21].
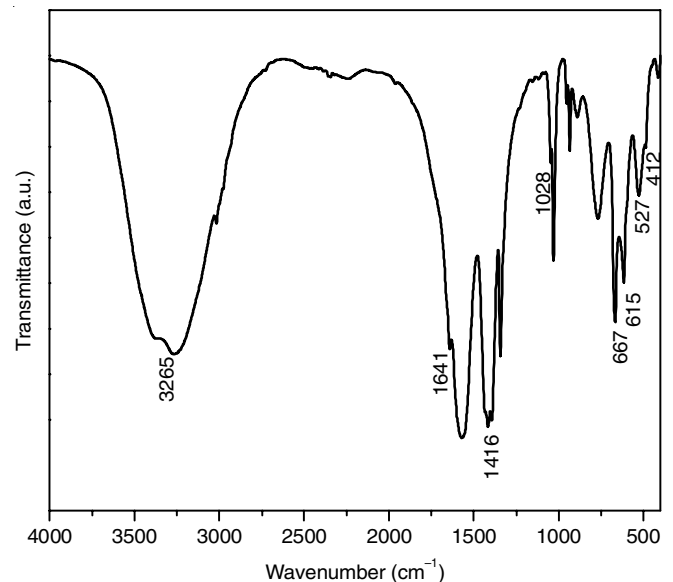

Fig. 4. FTIR spectrum for Mn_3O_4 nanoparticles

TABLE-1
CRYSTALLITE SIZE, LATTICE PARAMETERS, VOLUME, BOND LENGTH
AND STRAIN OF PURE MANGANESE OXIDE NANOPARTICLES

Sample	Lattice parameters (Å)		Crystallite size (nm)		Unit cell volume (Å)³	Bond length (Å)	Strain
	a = b	c	Debye scherrer's	W-H plot			
Mn_3O_4	5.7649	9.4541	26.1569	39	314.198	6.79	0.00169

A large band at 3265 cm^{-1} due to stretching vibrations of the -OH bond and the other bands at 1641, 1416 and 1028 cm^{-1} attributed to -OH bending modes. The FTIR spectrum indicates that water molecule present in the sample, which is very essential for function of battery [10].

Scanning electron microscope analysis: Fig. 5(a-d) represents the SEM images of the as-prepared Mn$_3$O$_4$ nanoparticles in different magnifications. The images indicate that the particles acquire irregular morphology and distributed with different sized particles. The particle sizes are not exactly same size, thus the average size of the particles are in the range 30 to 40 nm which is very agreed with the XRD results. The different sizes of nanoparticles are uniformly distributed and indicate the cluster of nanoparticles [10].
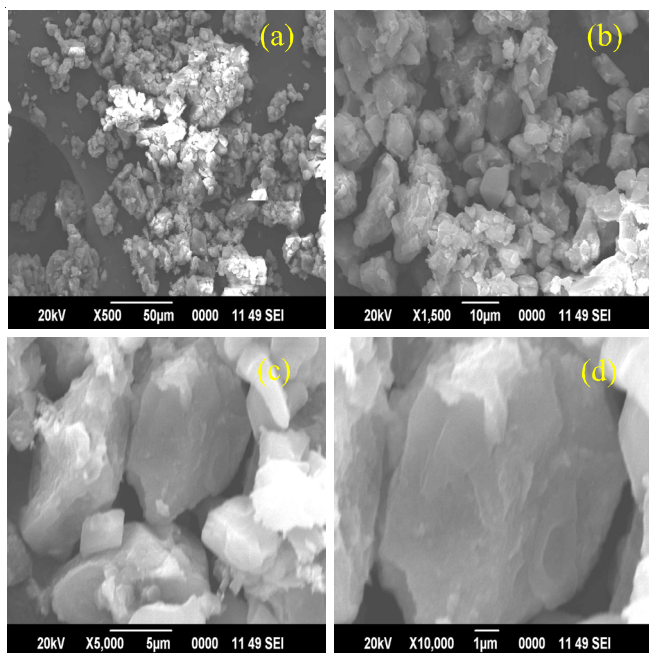

Fig. 5. SEM images for Mn$_3$O$_4$ nanoparticles

Optical studies by UV-visible spectrum: UV-visible spectrum illustrates that pure Mn$_3$O$_4$ nanoparticles exhibits maximum absorption at 396 nm, which is the effect of quantum confinement [22]. Direct band gap of Mn$_3$O$_4$ is determined by fitting the absorption data to the transition equation $(\alpha h\nu)^n = A(h\nu - E_g)$, where A is a constant, $h\nu$ is photon energy and α is the absorption coefficient while n = 2 for direct inter band transition.

Optical band gap energy E_g = 3.15 eV was obtained by extrapolating the linear part of the curve $(\alpha h\nu)^2$ *versus* photon energy $h\nu$ (eV) known as Tauc plot. Fig. 6 shows the ultraviolet-visible absorption spectra and inset of that figure represents Tauc plot for Mn$_3$O$_4$ nanoparticles.

Electrochemical properties by cyclic voltammogram: The electro chemical responses of the Mn$_3$O$_4$ was analyzed by cyclic voltammetry. This method examines the reversibility of as-synthesized nanosized Mn$_3$O$_4$ materials to the insertion and exsertion of the mobile ions. The cyclic voltammetry of the Mn$_3$O$_4$ electrodes measured in 1 M Na$_2$SO$_4$ electrolyte at scan rates of 50 mV s^{-1} by sweeping the potential -1.5 volt to 2.2 volt are shown in Fig. 7.
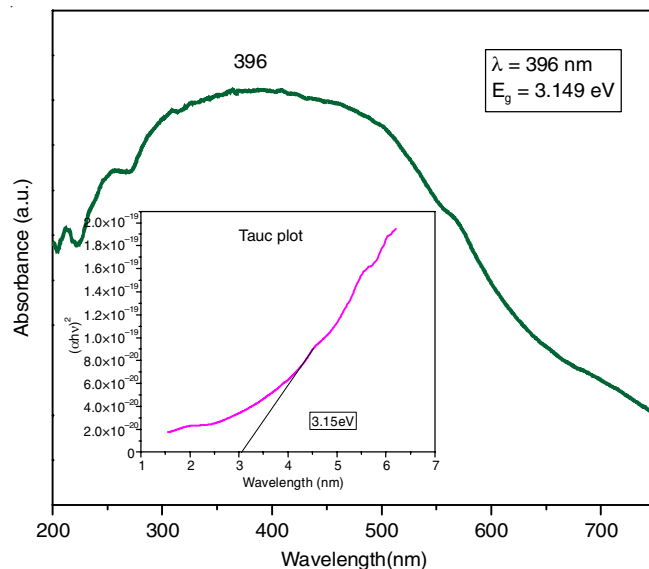

Fig. 6. UV-visible absorption spectra and Tauc plot for Mn$_3$O$_4$ nanoparticles
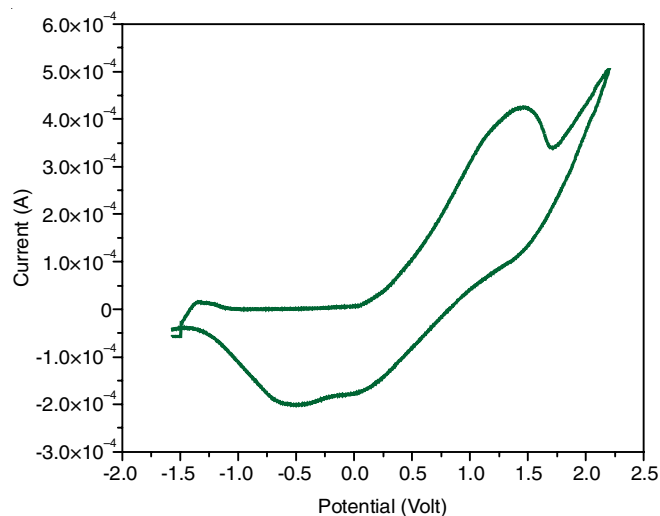

Fig. 7. Cyclic voltammogram of the Mn$_3$O$_4$ nanoparticles

The curves showing anodic and cathodic characteristic peaks, showed the pseudocapacitive activities and are different from ideal capacitor of rectangular shape. At first, the scan process run with sharp increase in the anodic peak (oxidation) at 1.2 volt and ends with broad cathodic peak at -0.4 volt. The metal oxide electrode can store the charges at the electrode or electrolyte interface and the redox reaction takes place in the alkaline electrolyte. The change in oxidation state due to the oxygen incorporated into the material.

The specific capacitance can be calculated from the CV curve by using formula:

$$C = \frac{1}{2rm(V_2 - V_1)} \int_{v1}^{v2} Idv$$

The specific capacitance of the electrodeposited Mn$_3$O$_4$ was found to be 3.46 F/g at the scan rate 50 mV s^{-1} in 1 M Na$_2$SO$_4$ electrolyte [23].

The charge-discharge curve of manganese oxide nanoparticles are shown in Fig. 8. This can be clearly seen that the charge-discharge curve is linear and symmetrical. It can be attributed to the rapid current-voltage response and a good electrochemical reversibility [24].
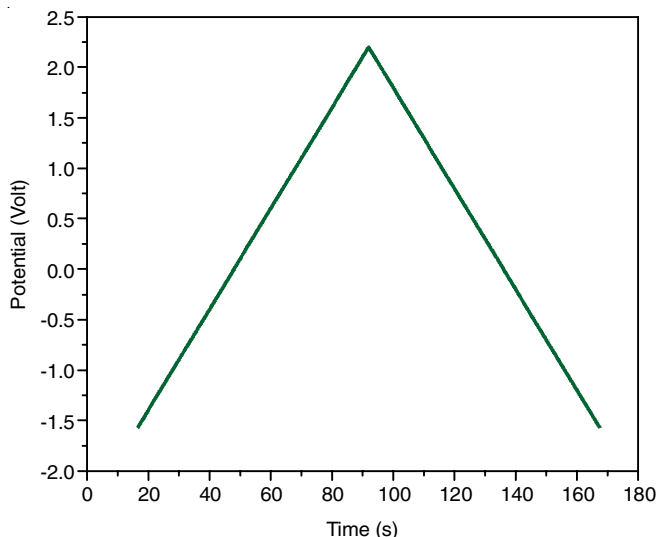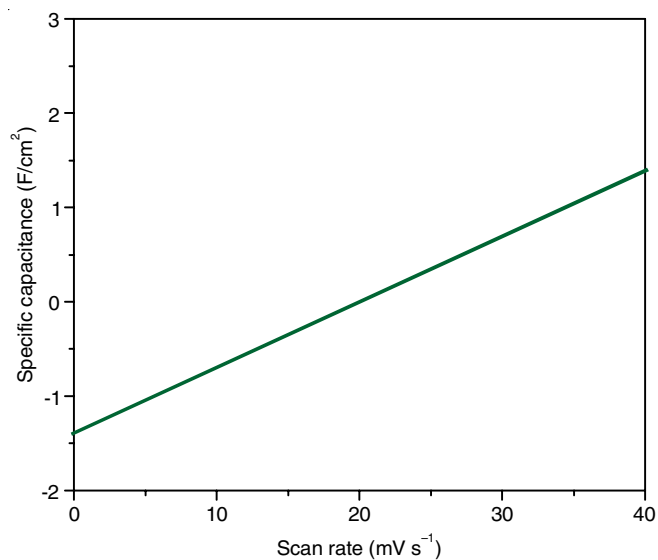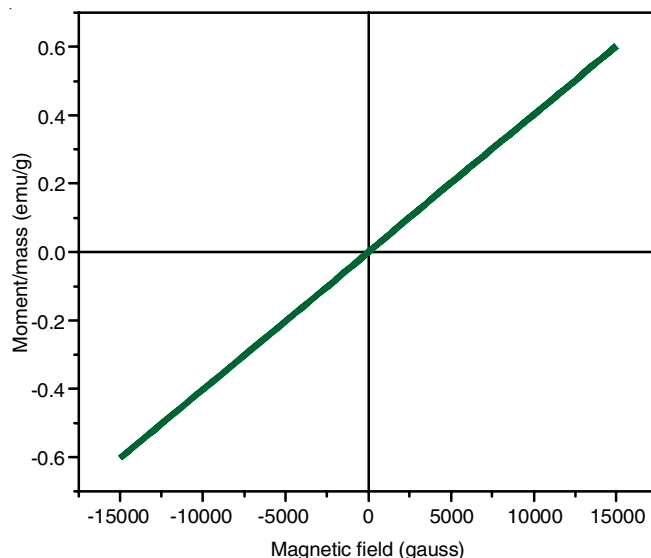
Fig. 8. Charge-discharge curve for Mn_3O_4 nanoparticles

Fig. 10. M-H curve for Mn_3O_4 nanoparticles

Fig. 9 represents the specific capacitance increases as the increasing scan rate. At high scan rates Na^+ ions reach the inner and outer surface of the electrode material. Mn_3O_4 fully involved in the electrochemical process [25,26].

Fig. 9. Scan rate-specific capacitance for Mn_3O_4 nanoparticles

Magnetic properties by VSM analysis: The M-H curves of as-synthesized Mn_3O_4 nanoparticles are linear with non-zero coercivity and retentivity (Fig. 10). The saturation magnetic moment is ±0.6 emu/g. The coercivity and retentivity and squareness ratio are recorded in Table-2.

At room temperature, the M-H curve indicates that as-synthesized nanoparticles exhibit superparamagnetic behaviour. When the particle size reduces, the atoms disordered on the surface. This result tends to decrease the magnetic moment [27]. When the size of the particle decreases, a multi domain transformed into single domain. If the single domain becomes very small, the magnetic moment within the domain changes in the direction due to thermal agitation. The thermal activation energy overcomes cohesive energy of changing magnetic domain which provides sufficient energy for the alignment of the particle magnetic moments in an applied magnetic field resulting in the suppression of hysterisis behaviour in the manganese oxide nanoparticles and then super paramagnetic behaviour exists [14].

Total magnetic isotropy: $K_{Tot} = K_{bulk} + K_{shape}$

The extrinsic property of magnetic material coercivity not only depends on spin but also on the size and shape of the particles. Due to decrease in anisotropy, the coercivity of Mn_3O_4 nanoparticles approach to minimum. The superparamagnetic behaviour of Mn_3O_4 nanoparticles assigned to decrease in the shape anisotropy of a system.

Conclusion

Mn_3O_4 nanoparticles are successfully synthesized with a single phase exists without core-shell structures. From the powder XRD results the crystallite size of the sample below 40 nm and is confirmed by SEM analysis. FTIR illustrates that the sample contains no foreign material only manganese and oxygen are present in the sample. The forbidden energy band gap of the Mn_3O_4 is 3.1 eV observed from UV-visible absorption spectra. From cyclic voltammogram exhibits Mn_3O_4 nanoparticle showed an excellent electrode material for super-capacitor applications. From magnetic studies, the size of the Mn_3O_4 particle reduces and then the disordered atomic structure on the surface increases. This tends to reduce the magnetic moment and also reduce the saturation magnetization.

CONFLICT OF INTEREST

The authors declare that there is no conflict of interests regarding the publication of this article.

TABLE-2 MAGNETIC PARAMETERS OF Mn_3O_4 NANOPARTICLES				
Sample	Coercivity (gauss)	Magnetization (emu/g)	Retentivity (memu/g)	Squareness ratio (SQR) $[M_r/M_s]$
Mn_3O_4	10.767	0.6023	0.4483	0.0007443

REFERENCES

1. K.K. Choudhary, Nonoscience and Nanotechnology, Narosa Publishing House: New Delhi (2016).

2. S. Xiong, W. Qi, Y. Cheng, B. Huang, M. Wang and Y. Li, *J. Phys. Chem.*, **13**, 10652 (2011);
https://doi.org/10.1039/c0cp90161j.

3. J. Rupp and R. Birringer, *Phys. Rev. B*, **36**, 7888 (1987);
https://doi.org/10.1103/PhysRevB.36.7888.

4. A. Akbarzadeh, M. Samiei and S. Davaran, *Nanoscale Res. Lett.*, **7**, 144 (2012);
https://doi.org/10.1186/1556-276X-7-144.

5. M. Sharrouf, R. Awad, M. Roumie and S. Marhaba, *J. Mater. Sci. Appl.*, **6**, 850 (2015);
https://doi.org/10.4236/msa.2015.610087.

6. R. Jothiramalingam and M.K. Wang, *J. Porous Mater.*, **17**, 677 (2011);
https://doi.org/10.1007/s10934-009-9338-8.

7. D. Jaganyi, M. Altaf and I. Wekesa, *J. Appl. Nanosci.*, **3**, 329 (2013);
https://doi.org/10.1007/s13204-012-0135-3.

8. A. Akbarzadeh, M. Samiei and S. Davaran, *J. Nanoscale Res. Letts.*, **7**, 144 (2012);
https://doi.org/10.1186/1556-276X-7-144.

9. A.M. Toufiq, F. Wang, Q. Javed, Q. Li and Y. Li, *J. Appl. Phys. A Mater. Sci. Process.*, **116**, 1127 (2014);
https://doi.org/10.1007/s00339-013-8195-0.

10. J.S. Sherin and J.K. Thomas, *Int. J. Sci. Eng. Appl.*, **4**, 250 (2015).

11. R. Shokoohi, M.T. Samadi, G. Asgari, Y. Poureshgh, M.V. Tabar, K. Godini and A. Shabanloo, *Avicenna J. Environ. Health Eng.*, (2015),
https://doi.org/10.17795/ajehe-8565.

12. G.A.M. Ali, L.L. Tan, R. Jose, M.M. Yusoff and K.F. Chong, *J. Mater. Res. Bull.*, **60**, 5 (2014);
https://doi.org/10.1016/j.materresbull.2014.08.008.

13. R. Song, H.-J. Wang and S.-H. Feng, *Chem. Res. Chin. Univ.*, **28**, 577 (2012).

14. J. Valencia, N. Arias-Duque, O. Giraldo and A. Rosales-Rivera, *Rev. Mex. Fis.*, **58**, 151 (2012).

15. N.J. Tharayil, R. Raveendran, A.V. Vaidyan and P.G. Chithra, *Indian J. Eng. Mater. Sci.*, **15**, 489 (2008).

16. N.J. Tharayil, R. Raveendran and A.V. Vaidyan, *Indian J. Pure Appl. Phys.*, **46**, 47 (2008).

17. Y. Luo, S. Fan, N. Hao, S. Zhong and W. Liu, *Dalton Transc.*, **43**, 15317 (2014);
https://doi.org/10.1039/C4DT01695E.

18. T. Theivasanthi and M. Alagar, *Nano Biomed. Eng.*, **4**, 58 (2012);
https://doi.org/10.5101/nbe.v4i2.p58-65.

19. H. Kumar, Manisha and P. Sangwan, *Int. J. Chem. Chem. Eng.*, **3**, 155 (2013).

20. F.Y. Cheng, J. Chen, X.L. Gou and P.W. Shen, *J. Adv. Mater.*, **17**, 2753 (2005);
https://doi.org/10.1002/adma.200500663.

21. Y.-S. Ding, X.-F. Shen, S. Gomez, H. Luo, M. Aindow and S.L. Suib, *J. Adv. Funct. Mater.*, **16**, 549 (2006);
https://doi.org/10.1002/adfm.200500436.

22. K.S. Pugazhvadivu, K. Ramachandran and K. Tamilarasan, *J. Phys. Procedia*, **49**, 205 (2013);
https://doi.org/10.1016/j.phpro.2013.10.028.

23. N. Elgrishi, K.J. Rountree, B.D. McCarthy, E.S. Rountree, T.T. Eisenhart and J.L. Dempsey, *J. Chem. Educ.*, **95**, 197 (2018);
https://doi.org/10.1021/acs.jchemed.7b00361.

24. B.C. Kim, C. Justin Raj, W.-J. Cho, W.-G. Lee, H.T. Jeong and K.H. Yu, *J. Alloys Compd.*, **617**, 491 (2014);
https://doi.org/10.1016/j.jallcom.2014.08.018.

25. B. Li, G. Gao, D. Zhai, C. Wei, Y. He, H. Du and F. Kang, *Int. J. Electrochem. Sci.*, **8**, 8740 (2013).

26. H.-M. Lee, K. Lee and C.-K. Kim, *J. Mater.*, **7**, 265 (2014);
https://doi.org/10.3390/ma7010265.

27. S. Zhang, W. Liu, J. Ma and Y. Zhao, *NSTI-Nanotech.*, **1**, 555 (2010).